



CHORUS

This is the accepted manuscript made available via CHORUS. The article has been published as:

Stabilization and current-induced motion of antiskyrmion in the presence of anisotropic Dzyaloshinskii-Moriya interaction

Siying Huang, Chao Zhou, Gong Chen, Hongyi Shen, Andreas K. Schmid, Kai Liu, and Yizheng Wu

Phys. Rev. B **96**, 144412 — Published 9 October 2017

DOI: [10.1103/PhysRevB.96.144412](https://doi.org/10.1103/PhysRevB.96.144412)

Stabilization and current-induced motion of antiskyrmion in the presence of anisotropic Dzyaloshinskii-Moriya interaction

Siyang Huang¹, Chao Zhou¹, Gong Chen^{2*}, Hongyi Shen¹, Andreas K. Schmid³, Kai Liu², and
Yizheng Wu^{1,4*}

¹Department of Physics and State Key Laboratory of Surface Physics, Fudan University, Shanghai 200433, People's
Republic of China

²Physics Department, University of California, Davis, California 95616, USA

³NCEM, Molecular Foundry, Lawrence Berkeley National Laboratory, Berkeley, California 94720, USA

⁴Collaborative Innovation Center of Advanced Microstructures, Nanjing 210093, China

Email: gchenncem@gmail.com, wuyizheng@fudan.edu.cn

Abstract:

Topological defects in magnetism have attracted great attention due to fundamental research interests and potential novel spintronics applications. Rich examples of topological defects can be found in nanoscale non-uniform spin textures, such as monopoles, domain walls, vortices, and skyrmions. Recently, skyrmions stabilized by the Dzyaloshinskii-Moriya interaction have been studied extensively. However, the stabilization of antiskyrmions is less straightforward. Here, using numerical simulations we demonstrate that antiskyrmions can be a stable spin configuration in the presence of anisotropic Dzyaloshinskii-Moriya interaction. We find current-driven antiskyrmion motion that has a transverse component, namely antiskyrmion Hall effect. The antiskyrmion gyroconstant is opposite to that for skyrmion, which allows the current-driven propagation of coupled skyrmion-antiskyrmion pairs without apparent skyrmion Hall effect. The antiskyrmion Hall angle strongly depends on the current direction, and a zero antiskyrmion Hall angle can be achieved at a critic current direction. These results open up possibilities to tailor the spin topology in nanoscale magnetism, which may be useful in the emerging field of skyrmionics.

I. Introduction

Topological defects such as monopoles, domain walls, vortices, and skyrmions play crucial roles in low dimensional magnetic systems [1], where topological features dominate their magnetic and dynamic properties. Examples include the switching of vortex core polarity via creation/annihilation of vortex - antivortex pair [2], magnetization reversal via soliton pair creation [3], topological protection of skyrmions [4] and domain walls [5]. Among these spin textures, magnetic skyrmions [6,7,8] have attracted increasing attention owing to the ultralow current density threshold to move them [9,10,11,12].

Magnetic skyrmions are nanometer-sized circular quasiparticles that have homo-chiral spin textures [4,12], where the nature of the magnetic chirality can be realized by several mechanisms, such as the antisymmetric exchange interaction, namely the Dzyaloshinskii-Moriya interaction (DMI) [13,14,15,16,17], four spin interactions [18], artificial confinement in patterned structures [19,20,21], or the competing exchange interactions [22,23]. In case of the DMI, broken inversion symmetry of the system is required as the interaction vanishes in symmetric systems. The DMI energy term can be written as $E_{DM} = -\mathbf{D}_{ij} \cdot (\mathbf{S}_i \times \mathbf{S}_j)$, where \mathbf{S}_i and \mathbf{S}_j are two spins on neighbouring atomic sites i and j , and \mathbf{D}_{ij} is the vector characterizing the DMI. Magnetic skyrmions have been observed experimentally in non-centrosymmetric bulk magnets [4,9,10,24,25], ultra-thin films where the inversion symmetry breaks at the interface [15,26,27,28,29,30], and artificial structures [19,20,21].

Experimental observations of magnetic skyrmion states have motivated studies on their creation [27,31], manipulation [31,32,33] and electric detection [34] in the presence of electric current [9,10,11,27,31,32] as well as magnetic field [9,10,11,27,28,29,30,31]. For possible skyrmionic memory and logic device applications envisioned so far, current-driven propagation of magnetic

47 skyrmions is highly relevant to device performance, with two key parameters being the critical
48 current for skyrmion propagation and the maximum propagation speed. Theoretical studies predict
49 that skyrmions propagate along trajectories away from the current direction due to the Magnus force
50 [4,35,36,37,38,39,40,41,42,43,44], following the so-called skyrmion Hall effect, which has been
51 recently observed in Néel-type skyrmions in thin film systems [45,46]. Theoretical studies have
52 further proposed that the skyrmion Hall effect can be suppressed by zeroing the net topological
53 charge in two coupled skyrmions with opposite topological charges, either in
54 antiferromagnetically-coupled trilayers with skyrmions on both sides [47], or in skyrmions in
55 antiferromagnetic materials [48].

56 Magnetic antiskyrmions are topologically non-trivial chiral spin quasiparticles that may occur
57 in cases where the magnetic chirality is anisotropic (as opposed to skyrmions with isotropic in-plane
58 chirality). They have received less attention up to now [4,49,50,51,52]. These theoretical works
59 predict that antiskyrmions can be stabilized in materials belonging to the crystallographic class D_{2d}
60 [53], as well as in frustrated exchange interaction systems [50] and in dipolar magnets [52].

61 In this work, we focus on the energetics of magnetic antiskyrmions in the presence of
62 anisotropic interfacial DMI, and further explore their electric current-driven dynamics. We provide a
63 phase diagram of spin configurations including skyrmions, antiskyrmions and multidomains (spin
64 spirals) in a 2D space of the DMI vector along two orthogonal in-plane directions. We show that the
65 topological charge of the antiskyrmions may also induce a Magnus force-associated propagation
66 deviation, i.e. an antiskyrmion Hall effect. Moreover, we find that the anisotropic spin texture of
67 antiskyrmions gives rise to significant anisotropy in the skyrmions' response to applied electric
68 current, i.e. the antiskyrmion Hall angle (between propagation direction and current direction)

69 strongly depends on the applied current direction with respect to the internal spin texture of
70 antiskyrmions. Indeed the antiskyrmion Hall angle ranged from positive to negative, even crossing
71 zero degree for certain current directions. This tunability of the antiskyrmion Hall angle is a new
72 degree of freedom that enables the control of trajectories of topological quasiparticles, which might
73 be useful in skyrmionics-based memory or logic devices. We also investigate the current-driven
74 dynamics of a coupled skyrmion-antiskyrmion pair in which the Magnus force of the skyrmion and
75 antiskyrmion can be cancelled.

76 **II. Stabilization of antiskyrmions by anisotropic DMI**

77 We first discuss differences in the mechanisms that stabilize skyrmions and antiskyrmions. At
78 the interface between a thin magnetic film and a heavy metal adjacent layer the DM vector \mathbf{D}_{ij}
79 between spins \mathbf{S}_i and \mathbf{S}_j on atomic sites i and j usually lies within the film plane and normal to
80 the distance vector \mathbf{r}_{ij} [17,18]. Note that the orientation of the \mathbf{D}_{ij} vector plays a critical role in
81 determining the chiral spin configuration. Generally, skyrmion configurations result from isotropic
82 interfacial DMI [17,18,26,27,28,29,30,31], i.e. in systems where the \mathbf{D}_{ij} vector is either parallel or
83 antiparallel to $\mathbf{z} \times \mathbf{r}_{ij}$, where \mathbf{z} is interface normal direction [17]. For instance, in a four-fold
84 symmetric system such as an fcc(001) interface, four \mathbf{D}_{ij} vectors at four j sites ($j = 1,2,3,4$)
85 adjacent to an atom at site i (see Fig. 1(a)) can be written as $\mathbf{D}_1 = D_1 \hat{\mathbf{y}}$, $\mathbf{D}_2 = -D_2 \hat{\mathbf{x}}$, $\mathbf{D}_3 = -D_3 \hat{\mathbf{y}}$,
86 $\mathbf{D}_4 = D_4 \hat{\mathbf{x}}$, respectively, where D_j is strength of the DMI vector on j sites, and $\hat{\mathbf{x}}$ and $\hat{\mathbf{y}}$
87 correspond to the unit vector along the x and y axis, respectively. The DMI vectors on opposite j
88 sites are opposite, i.e. $\mathbf{D}_1 = -\mathbf{D}_3$, and $\mathbf{D}_2 = -\mathbf{D}_4$, so for simplicity we discuss the DMI vector
89 configurations in $D_1 - D_2$ space in the rest of the paper. Most previous studies usually assumed that
90 the interfacial DMI vectors on four j sites have the same rotational sense [17], e.g. the DMI vector

91 configuration shown in Fig. 1(a), resulting in same chirality along all in-plane directions (Fig. 1(c)).
92 Note that flipping the sign of all DMI vectors will reverse the magnetic chirality within skyrmions,
93 but the topological charge remains the same for both chiralities when the cores of skyrmions point in
94 the same direction (Fig. 1(e)) [4].

95 In most previous studies it has always been assumed that the strengths of D_1 and D_2 are equal,
96 a view that is generally accepted in systems with four-fold symmetry and in polycrystalline systems.
97 In contrast, atomic configurations with broken in-plane rotation symmetry at the interface may lead
98 to anisotropic interfacial DMI [17]. For instance, first principles calculations predict that the bcc
99 Fe/W(110) interface has opposite \mathbf{D}_{ij} vectors along two orthogonal in-plane directions [001] and
100 $[1\bar{1}0]$ [54]. Recently, anisotropic DMI was experimentally observed at the Co/W(110) interface,
101 where the strength of the DMI \mathbf{D}_{ij} vector was found to have the same sign but 2.5 times stronger
102 magnitude along the bcc $[1\bar{1}0]$ direction compared to the orthogonal direction bcc [001] [55]. Note
103 that the in-plane anisotropy of the DMI vector \mathbf{D}_{ij} changes the energy landscape of chiral spin
104 textures along different in-plane direction. For instance antiskyrmions are stabilized when the \mathbf{D}_{ij}
105 vectors along x and y directions have opposite sign, i.e. along the vertical direction in the sketch in
106 Fig. 1(b) the vectors remain the same as in Fig. 1(a) ($\mathbf{D}_1 = D_1\hat{\mathbf{y}}$), but along the horizontal direction
107 vectors flip their sign ($\mathbf{D}_2 = D_2\hat{\mathbf{x}}$ instead of $\mathbf{D}_2 = -D_2\hat{\mathbf{x}}$). This anisotropic DMI configuration
108 favours opposite chirality along x and y direction, which allows the stabilization of magnetic
109 antiskyrmions (Fig. 1(d)). Note that the energies of dipolar interaction between skyrmions and
110 antiskyrmions are slightly different due to the different length fraction of Néel- vs. Bloch-type
111 domain walls on their boundaries. However the dipolar energies of opposite Néel-type (or
112 Bloch-type) chiralities are degenerate [56,57], therefore dipolar interactions do not influence the

113 **anisotropic chirality of the antiskyrmions.** Note also that the antiskyrmion shown in Fig. 1(f) carries
114 the opposite topological charge compared to the skyrmion sketched in Fig. 1(e) [4].

115 Next we discuss the possibility to stabilize antiskyrmions in nanodisks in the presence of
116 anisotropic interface DMI. We performed micromagnetic simulations using the OOMMF code
117 including the DMI [58,59], and numerically calculated the relaxed micromagnetic state of
118 80-nm-wide 0.4nm thick nanodisks in zero field. As described in more detail in the Methods section,
119 our model captures the DMI strengths of D_1 and D_2 in terms of the area unit energy densities D_x
120 and D_y . In the simulations, plausible initial states of antiskyrmions, quasi-uniform and multidomain
121 magnetization distributions are relaxed to obtain different final states (see Methods). We first assume
122 that the DMI vectors (D_x, D_y) have the same magnitude and opposite sign, i.e. $D_x = -D_y$. Figure
123 2(a) shows the total micromagnetic energy of three possible configurations as a function of D_x ,
124 including a quasi-uniform state (red circles), antiskyrmion state (black squares) and 2π -rotation state
125 (blue triangles, explained below) [60]. It is clear that for $D_x < D'$, the most stable state is
126 quasi-uniform state with tilted spins at the edge, consistent with results reported in Ref. 60. The
127 antiskyrmion state becomes the ground state when $D' < D_x < D''$, where the size of antiskyrmions
128 increases with the magnitude of D_x . For $D_x > D''$, the most favoured state is a 2π -rotation state with
129 the spins rotating by 2π from the center to the edge of the disk, and for stronger D_x , $n\pi$ -rotation
130 states with $n > 2$ may exist. **Skyrmion textures with isotropic chirality** are not discussed here
131 because their DMI energy would far exceed that of antiskyrmions in the anisotropic DMI case.
132 Figure 2(b) shows a typical spin configuration of a stable antiskyrmion with $D_x = -D_y = 4 \text{ mJ m}^{-2}$.

133 **III. Simulated spin texture phase diagram in an anisotropic DMI system**

134 It is interesting to explore further the spin configurations of such nanodisks under conditions

135 where D_x and D_y are unbalanced [54,55]. A phase diagram shown in Fig. 3(a) summarizes the
136 dependence of spin texture ground states of the disk in (D_x, D_y) space (see details in Methods),
137 where the (D_x, D_y) quadrant represents isotropic chirality states containing skyrmion configurations,
138 and the $(D_x, -D_y)$ quadrant represents anisotropic chirality states containing antiskyrmion
139 configurations. The shapes of skyrmions (cyan region in the phase diagram) and antiskyrmions
140 (yellow region) evolve from circular (Fig. 3(b) and 3(c)) to elliptical (Fig. 3(d) and 3(e)) when the
141 magnitude of D_x and D_y are unequal. **Note that such elliptical deformation may also be present in**
142 **a biaxial magnetic anisotropy system [61].** The quasi-uniform out-of-plane ferromagnetic states
143 (darker cyan and darker yellow regions) have tilted spins at the edge due to the presence of the DMI
144 [60]. Depending on the magnitude of D_x and D_y , multi-domain ground states either form stripe-like
145 phases (Fig. 3(f) and 3(g)) or $n\pi$ -rotation phases (Fig. 3(h) and 3(i) shows the spin texture with
146 $n = 2$),

147 **IV. Current-induced motion of antiskyrmions in nanotracks**

148 Exploring the dynamical properties of antiskyrmions is fundamentally interesting, as these
149 objects are a unique type of topologically charged quasiparticles. In this section we explore, by
150 micromagnetic simulations, current-induced motions of skyrmions and antiskyrmions confined
151 within nanotracks. For these simulations we implemented in the OOMMF code additional torque
152 terms added to the LLG equation (see Methods) [58,59]. A spin current polarized along +y
153 direction is injected vertically by the spin Hall effect [11,60]. We simulated both skyrmions, under
154 isotropic DMI (D_x, D_y) , and antiskyrmions with equivalent size under anisotropic DMI $(D_x, -D_y)$.
155 To highlight the importance of topology, the magnitudes of D_x and D_y are always kept to
156 $3 \text{ mJ } m^{-2}$ in this section. Simulations show that skyrmions and antiskyrmions propagate with the

157 same velocity under a driving current density $j = 1 \text{MA cm}^{-2}$ (Fig. 4(a) and Supplementary Movie
158 1 in ref. 62), and their velocities parallel to the nanotrack increase linearly with the current density.
159 With higher current density, both skyrmion and antiskyrmion show a transverse velocity in the
160 y-direction.

161 The transverse motions for skyrmion and antiskyrmion are in opposite directions. This is
162 understood within the picture of the Thiele equation as used to describe skyrmion Hall effect in rigid
163 skyrmion systems [4,38,43,44,43,45],

$$164 \quad \mathbf{G} \times \mathbf{v} - \alpha \mathbf{D} \cdot \mathbf{v} - 4\pi \mathbf{B} \cdot \mathbf{j} = 0 \quad (1)$$

165 where $G = (0,0,-4\pi Q)$ is the gyromagnetic coupling vector, and the skyrmion and antiskyrmion
166 have opposite topological charge Q ; $\mathbf{v} = (v_x, v_y)$ is the propagation velocity along the x and y
167 axis, respectively; α is the Gilbert damping coefficient, and \mathbf{D} is the dissipative force tensor. The
168 tensor \mathbf{B} represents the efficiency of the spin Hall torque over the skyrmion/antiskyrmion, and \mathbf{j} is
169 the electric current density flowing in the heavy metal. The first term in Eq. (1) is the topological
170 Magnus force [41,45], which induces the transverse motion of skyrmions (or anitskyrmion) with
171 respect to the driving current. The second term is the dissipative force due to the magnetic damping
172 of a moving magnetic skyrmion (or antiskyrmion), and the third term shows the driving force from
173 the spin Hall torque. The Thiele equation yields $v_x = \frac{-j\alpha D B_{xx}}{(\alpha D)^2 + Q^2}$ and $v_y = \frac{jQ B_{xx}}{(\alpha D)^2 + Q^2}$ for the velocity
174 components of the skyrmion or antiskyrmion along x and y direction (see Methods), showing that
175 the opposite transverse motion v_y of skyrmion and antiskyrmion is due to their opposite topological
176 charge Q . Such transverse motion stops near the edge of the nanotrack due to the repulsive
177 interaction caused by the tilting magnetization at the edge induced by DMI [11,35]. (The propagation
178 without the edge effect will be discussed in next section.) Just as the topological properties of

179 skyrmions can reduce the influence of defects on their motion, our simulations suggest that
180 antiskyrmions are equally protected from defect-induced perturbations by their topological order (see
181 Supplementary Figure 1 and movie 2 in ref. 62). When the driving current is sufficiently strong, the
182 transverse force on either skyrmions or antiskyrmions is sufficient to overcome the repulsive barrier
183 at the track edge, resulting in annihilation. In the case of antiskyrmions this annihilation occurs
184 earlier than in the case of skyrmion under the similar conditions (Fig. 4(a)). This is because
185 antiskrymions can be slightly rotated by the spin-orbit torque during their motion – consequently,
186 when antiskyrmions approach the track-edge as a result of strong spin current, the radial component
187 of magnetization near the track edge is reduced and causes a weaker repulsive interaction between
188 the antiskyrmion and the edge.

189 **V. Anisotropic antiskyrmion Hall effect.**

190 Inspired by theoretical predictions and experimental observations of the skyrmion Hall effect
191 [4,35,36,37,38,39,40,41,42,45,46,47,48], we investigate whether antiskyrmions may also exhibit
192 current-driven transverse motion associated with their anisotropic spin texture. Figures 5(a) and 5(b)
193 show the typical propagation trajectories of a single skyrmion and antiskyrmion stabilized by
194 identical DMI vector magnitudes (the amplitude of both D_x and D_y are set to 3 mJ m^{-2}) in the
195 presence of current density of $j = 10 \text{ MA cm}^{-2}$ along the x direction (see Supplementary Movies
196 3 and 4 in ref. 62). One feature is that, without the edge effect, the transverse motions of skyrmions
197 and antiskyrmions are in opposite directions (along y axis) while they are both propagating along
198 $+x$ direction. These transverse motions can be quantified as the skyrmion/antiskyrmion Hall angle,
199 i.e. the relative angle from the applied current to the motion trajectory direction, which can be
200 calculated from the ratio of v_y/v_x . We found that both the skyrmion and antiskyrmion Hall angles

201 are equal to $\arctan(-\frac{Q}{\alpha D})$, thus they have the opposite values due to the opposite topological charge
 202 Q , and the value increases with the DMI strength, supported by both calculation and simulation (Fig.
 203 5(e)).

204 In contrast to skyrmions in which the spin texture is isotropic, antiskyrmions have anisotropic
 205 in-plane spin textures. In the following we explore the possible anisotropic responses when current is
 206 injected in arbitrary directions θ with respect to the $+x$ axis. The θ angle dependent skyrmion
 207 Hall angle and antiskyrmion Hall angle can also be understood in the picture of the modified Thiele
 208 equation. The derived skyrmion Hall angle equals to $\arctan(-\frac{Q}{\alpha D})$, independent of θ , whereas the
 209 antiskyrmion Hall angle equals $\arctan(-\frac{Q}{\alpha D}) - 2\theta$ (Methods), so the antiskyrmion Hall angle
 210 rotates oppositely against the rotation of angle θ . Simulation in Fig. 5(c) indeed shows that the
 211 antiskyrmion Hall angle changes its sign (being positive with respect to current direction) when the
 212 current is injected along the $-y$ direction ($\theta = -90^\circ$) (see Supplementary Movie 5 in ref. 62). This
 213 θ -dependent sign change of the antiskyrmion Hall angle gives rise to opportunities to tailor the
 214 trajectories of antiskyrmions in the presence of electric current. Moreover, the transverse motion of
 215 antiskyrmions can be eliminated when current is injected at the angle $\theta = \arctan(-\frac{Q}{\alpha D})/2$. This
 216 allows for the propagation of antiskyrmions along the current direction with zero Hall effect, which
 217 is supported by the simulation shown in Fig. 5(d) and Supplementary Movie 6 in ref. 62, where the
 218 θ angle equals to -34.5° . Figure 5(f) shows the simulated linear dependence of antiskyrmion Hall
 219 angle on θ with current density of $j = 10 \text{ MA cm}^{-2}$ (see additional angle dependence in
 220 Supplementary Movies 7 and 8 in ref. 62), which can be well fitted by the antiskyrmion Hall angle of
 221 $\arctan(-\frac{Q}{\alpha D}) - 2\theta$ derived from the Thiele equation. The total velocity of antiskyrmion
 222 $v = \frac{B_{xx}}{\sqrt{(\alpha D)^2 + Q^2}} |\mathbf{j}|$ is independent of the angle θ . We found that the critical current direction with

223 zero antiskyrmion Hall angle depends on the DMI strength, and also shows little current dependence
224 for $j < 20 \text{ MA cm}^{-2}$, but could change obviously at larger current density and reach -33.1° with
225 $j = 50 \text{ MA cm}^{-2}$. This is because the spin configuration in antiskyrmions can be modified by the
226 spin torque under strong spin current, resulting in the size change of antiskyrmions (see
227 Supplementary Figure 2 in ref. 62).

228 We expect that this unique property could significantly benefit the design of spintronic devices
229 based on skyrmions and antiskyrmions. As shown in Fig. 4(b), the maximum velocity of a single
230 skyrmion or antiskyrmion is typically less than 100 m s^{-1} , limited by the competition between the
231 skyrmion/antiskyrmion Hall effect and the edge confining force [11,37,47]. By patterning a
232 nanotrack along the direction enabling zero antiskyrmion Hall angle as shown in Fig. 5(d), the
233 maximum velocity of antiskyrmions can potentially be greatly increased, allowing a faster and
234 denser design of data technologies based on antiskyrmions.

235 **VI. Coupled antiskyrmion-skyrmion pairs without skyrmion Hall effect.**

236 Due to the skyrmion Hall effect, magnetic skyrmions may be annihilated at the edges of
237 nanotracks in the presence of a significant current (Fig. 4(a)), this effect limits the skyrmion motion
238 speed in nanotracks. It was proposed that the skyrmion Hall effect can be efficiently suppressed by
239 building pairs of antiferromagnetically exchange-coupled skyrmions in trilayer systems, where the
240 Magnus forces on the two skyrmions are cancelled due to opposite topological charge Q [47].
241 Considering the opposite Q for skyrmion and antiskyrmion, we propose that the transverse motion
242 of a current-driven ferromagnetically coupled antiskyrmion-skyrmion pair can be eliminated as well
243 (see the sketch of the structure in Fig. 6(a)). When coupled by interface ferromagnetic exchange
244 interaction across the spacer layer, both the antiskyrmion in the top layer and the skyrmion in the

245 bottom layer can be stabilized in the track (Methods). Note that the calculated sizes of the coupled
246 antiskyrmion and skyrmion are equal, but decrease with the interface exchange energy σ . When σ
247 increases up to 0.12 mJ m^{-2} , the coupled antiskyrmion-skyrmion pair becomes unstable (see
248 Supplementary Figure 3 in ref. 62).

249 We injected a current with the density $j = 5 \text{ MA cm}^{-2}$ in the track. With weak interlayer
250 coupling for $\sigma < 0.015 \text{ mJ m}^{-2}$, antiskyrmion and skyrmion move along the track with the opposite
251 transverse motion due to the opposite topological charge (see Fig. 6(c) and Supplementary Movie 9
252 in ref. 62). Because of the interface exchange coupling, the angle between their trajectories and x
253 direction has been significantly reduced compared to the skyrmion Hall angle in the single skyrmion
254 configuration. While skyrmion and antiskyrmion move more apart from each other, they eventually
255 decouple and move to track edges separately. Our simulation reveals that the decoupling of the
256 skyrmion-antiskyrmion pair happens later for stronger σ , and the decomposition distance of the
257 skyrmion-antiskyrmion pair has a dramatic increase for $\sigma \sim 0.015 \text{ mJ m}^{-2}$ with a current density of
258 $j = 5 \text{ MA cm}^{-2}$, as shown in Fig. 6(b). For $\sigma > 0.016 \text{ mJ m}^{-2}$, the antiskyrmion-skyrmion pair will
259 move parallel along the applied current direction synchronously (Fig. 6(d) and Supplementary Movie
260 10 in ref. 62). As shown in Fig. 4b, the maximum velocity of a single skyrmion or antiskyrmion is
261 typically less than 10^2 m s^{-1} , limited by the edge confining force. The maximum velocity of a
262 coupled skyrmion-antiskyrmion pair is much larger than a single skyrmion or antiskyrmion, and the
263 pair can move along the central line of the nanotrack at a high speed of a few hundred meters per
264 second, making this system a good candidate to utilize the skyrmions or antiskyrmions in confined
265 geometries.

266 VII. Conclusion

267 In summary, we have studied the effect of anisotropic antisymmetric exchange interaction on the
268 chiral spin textures by numerical simulations. We find that magnetic antiskyrmions can be stabilized
269 in nanodisks in the presence of anisotropic interfacial DMI. A phase diagram of chiral spin textures is
270 shown, including skyrmion and antiskyrmion in the disk, in the absence of applied magnetic field.
271 Current-driven propagation of antiskyrmions contains a transverse component due to the Magnus
272 force associated with the topological charge, opposite to the transverse motion of skyrmions.
273 Moreover, the antiskyrmion Hall angle strongly depends on the direction of the applied current with
274 respect to the in-plane spin structures of antiskyrmions. This constitutes a new degree of freedom to
275 manipulate the trajectories of **chiral spin textures**, and enables the design where antiskyrmion
276 propagation is free of transverse motion. We further show that coupling an antiskyrmion-skyrmion
277 pair in a trilayer structure is an alternative approach to suppress the topological charge-associated
278 Magnus forces. These results may trigger experimental efforts to explore antiskyrmions, and the
279 current-driven dynamics of antiskyrmions has exciting potentials for novel functionalities.

280 VIII. Methods

281 A. Micromagnetic modelling

282 In this study, we considered a 0.4-nm-thick perpendicularly magnetized cobalt film grown on a
283 substrate inducing anisotropic DMI. In a continuous magnetization model, the DMI energy can be
284 expressed as:

$$285 \quad \varepsilon_{DM} = D_x \left(m_z \frac{\partial m_x}{\partial x} - m_x \frac{\partial m_z}{\partial x} \right) + D_y \left(m_z \frac{\partial m_y}{\partial y} - m_y \frac{\partial m_z}{\partial y} \right) \quad (2)$$

286 where m_x, m_y, m_z are the components of the unit magnetization. D_x and D_y are area unit energy
287 densities related to the strength of D_1 and D_2 shown in Fig. 1, with a $1/at$ proportional factor,
288 where a is the atomic lattice constant and t is film thickness [11].

289

B. Simulations of the ground state

290 The simulations of this finite micromagnetic system were done using the modified OOMMF
 291 code including the anisotropic DMI [58,59]. We first investigated the relaxed state of an 80nm wide,
 292 0.4nm thick nanodisk on a substrate in zero field. We used perpendicular magnetic anisotropy
 293 $K = 0.6 \text{ MJ m}^{-2}$ along the z axis, exchange stiffness $A = 1.5 \text{ pJ m}^{-1}$, Gilbert damping $\alpha = 0.3$
 294 and saturation magnetization $M_s = 580 \text{ kA m}^{-1}$, similar to the parameters used in Ref. 11. The unit
 295 cell in the simulation is $0.4 \times 0.4 \times 0.4 \text{ nm}^3$. To obtain the total energies of the quasi-uniform states,
 296 antiskyrmion states and 2π -rotation states as a function of D_x , as summarized in Fig. 2(a), we first
 297 set initial spin configurations corresponding to these states and then relax the system to the final
 298 states. To obtain the phase diagram in (D_x, D_y) space shown in Fig. 3(a), we initially set the
 299 magnetization in the central 20nm diameter region along the $+z$ direction and set the magnetization
 300 outside of the 20nm diameter along the $-z$ direction, and then relaxed the magnetic system from
 301 the initial state by solving Landau-Lifschitz-Gilbert (LLG) equation step-by-step.

302

C. Simulations of current-driven skyrmion/antiskyrmion propagations

303 To simulate current-driven motions of skyrmions and antiskyrmions by the vertical injection of
 304 spin current (as it occurs by spin Hall effect in magnetic films grown on heavy metals with large spin
 305 Hall angle), we used the OOMMF code including extra torques terms added to the LLG equation
 306 [11,59]:

$$307 \quad \boldsymbol{\tau}_1 = -\gamma\tau_1(\hat{\mathbf{m}} \times \hat{\boldsymbol{\sigma}} \times \hat{\mathbf{m}}) \quad (3)$$

$$308 \quad \boldsymbol{\tau}_2 = -\gamma\tau_2(\hat{\mathbf{m}} \times \hat{\boldsymbol{\sigma}}) \quad (4)$$

309 where $\boldsymbol{\tau}_1$ is the in-plane torque and $\boldsymbol{\tau}_2$ is the out-of-plane torque with τ_1 and τ_2 being torque
 310 magnitudes. $\hat{\mathbf{m}}$ is the unit vector along the magnetization axis, $\hat{\boldsymbol{\sigma}}$ is direction of the current

311 polarization vector and γ is the gyromagnetic ratio. As shown in Ref. 11, for films thinner than the
312 absorption length of spin transfer, incomplete spin transfer of the injected spin current can be taken
313 into account by a renormalized spin polarization P , and we used the value of $P=40\%$ in our
314 simulations. In simulations of current-induced motion of skyrmions and antiskyrmions, the unit cell
315 is $1 \times 1 \times 0.4\text{nm}^3$.

316 For current-induced motion in nanotracks, the cross-section of the nanotrack is $40\text{ nm} \times$
317 0.4 nm . To obtain antiskyrmions and skyrmions with reduced diameters, the anisotropy K in this
318 simulation was set to 0.8 MJ m^{-2} . A spin current polarized along the $+y$ direction is injected from
319 the heavy metal layer along the z direction to the Co layer due to the spin Hall effect [11,60]. To
320 simulate the antiskyrmion Hall effect under various applied current directions, we used a sufficiently
321 large square thin film ($300\text{ nm} \times 300\text{ nm} \times 0.4\text{ nm}$) to avoid edge effects. The skyrmion (or
322 antiskyrmion) is initially positioned at the center of the track to reduce the influence from the edge
323 magnetization. In the simulation of current-driven antiskyrmion-skyrmion pair motion, we used a
324 trilayer track of $80\text{ nm} \times 1.2\text{ nm}$ cross section (the thicknesses of top layer, spacer layer and
325 bottom layer are all 0.4 nm). The increased width of 80 nm is used here to reduce the influence of
326 track edges so that the transverse motions can be clearly observed. In the top layer, the anisotropic
327 DMI is set to $D_x = -D_y = 3\text{ mJ m}^{-2}$, and in the bottom layer the isotropic DMI is set to $D_x =$
328 $D_y = 3\text{ mJ m}^{-2}$.

329 **D. Current-direction dependent antiskyrmion Hall effect**

330 To understand the anisotropic skyrmion/antiskyrmion Hall angle, we start from the modified Thiele
331 equation $\mathbf{G} \times \mathbf{v} - \alpha \mathbf{D} \cdot \mathbf{v} - 4\pi \mathbf{B} \cdot \mathbf{j} = 0$, where the dissipative force tensor \mathbf{D} is determined by the
332 spin configuration in skyrmion or antiskyrmion, which is given by $\mathbf{D} = D_{xx} = D_{yy} =$

333 $\int_{UC}(\partial_i \mathbf{m} \cdot \partial_j \mathbf{m}) dx dy$ and $D_{xy} = D_{yx} = 0$ for both skyrmion and antiskyrmion configurations.
 334 The tensor $\mathbf{B} = \begin{pmatrix} B_{xx} & 0 \\ 0 & B_{yy} \end{pmatrix}$ can be determined by the detailed spin configuration and the
 335 topological charge Q , with $B_{xx} = B_{yy}$ for skyrmion and $B_{xx} = -B_{yy}$ for antiskyrmion.
 336 $\mathbf{v} = (v_x, v_y)$ is the drift velocity of skyrmion or antiskyrmion along the x and y axis, respectively.
 337 $\mathbf{j} = (j \cos \theta, j \sin \theta)$ is the electrical current density flowing in the heavy metal, where j is the
 338 magnitude of the applied current density and θ is the relative angle between the current and the x
 339 axis. Now the Thiele equation yields

$$340 \quad \begin{cases} v_x = \frac{j}{(\alpha D)^2 + Q^2} (-\alpha D B_{xx} \cos \theta - Q B_{yy} \sin \theta) \\ v_y = \frac{j}{(\alpha D)^2 + Q^2} (Q B_{xx} \cos \theta - \alpha D B_{yy} \sin \theta) \end{cases} \quad (5)$$

341 Therefore the skyrmion Hall angle and antiskyrmion Hall angle can be calculated by the ratio of
 342 v_y/v_x , where the skyrmion Hall angle is $\arctan(-\frac{Q}{\alpha D})$, and the antiskyrmion Hall angle is
 343 $\arctan(-\frac{Q}{\alpha D}) - 2\theta$ (see details in Supplementary Note 1 in ref. 62). The total velocity for both
 344 skyrmion and antiskyrmion is $v = \frac{B_{xx}}{\sqrt{(\alpha D)^2 + Q^2}} j$.

345 *Note added.* After the original submission of this work, two relevant studies have appeared.
 346 Nayak *et al.* [63] reported an observation of magnetic antiskyrmions above room temperature in
 347 tetragonal Heusler materials with D_{2d} symmetry, and Hoffmann *et al.* [64] reported the possibility of
 348 stabilizing antiskyrmions in (110) oriented ultrathin films with C_{2v} symmetry.

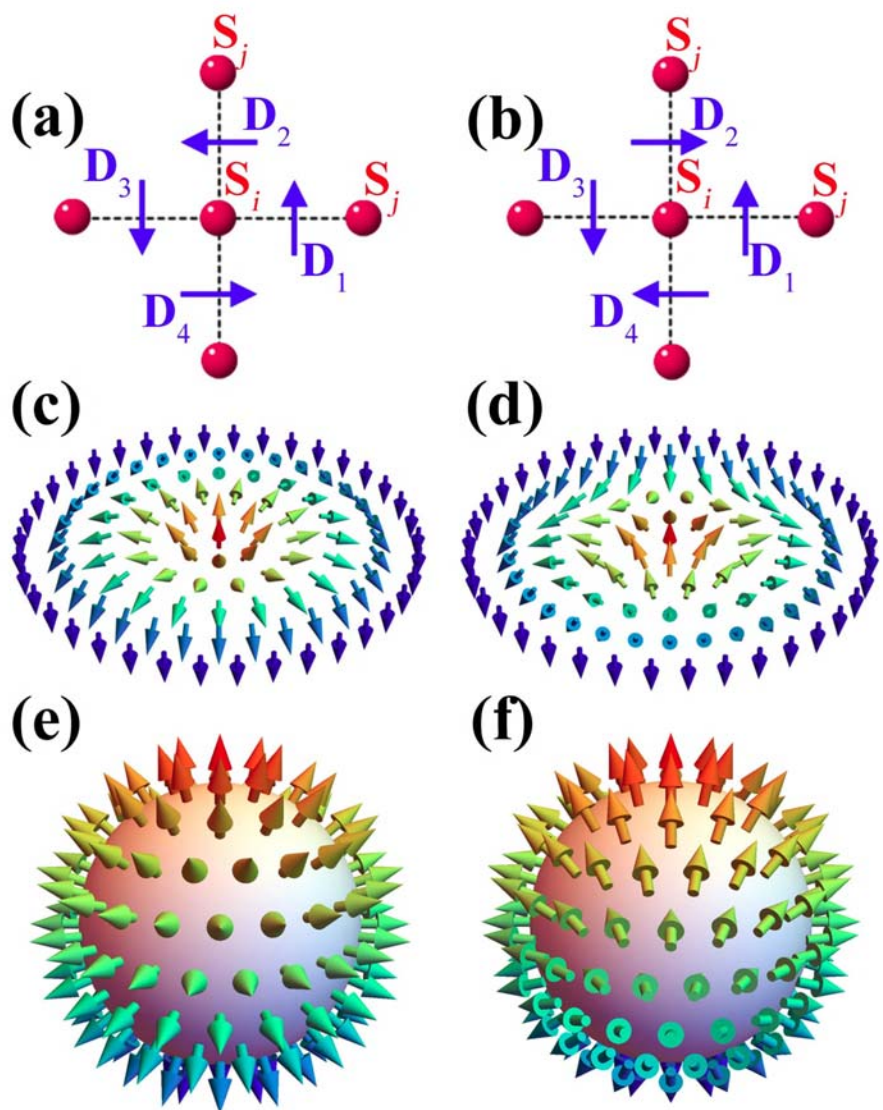
349

350

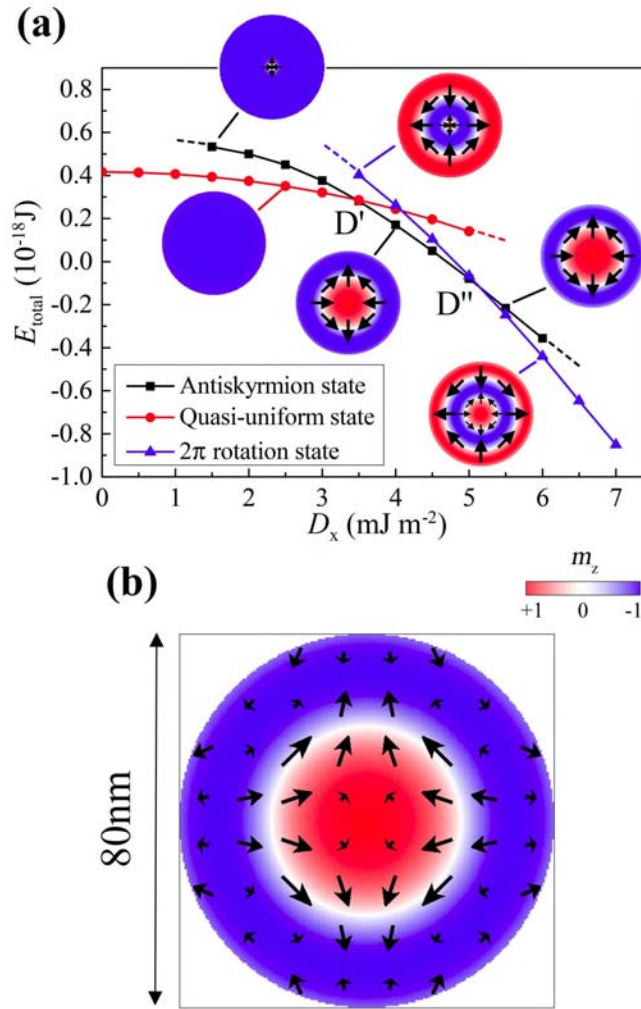
Acknowledgements

351 This work was supported by the National Key Basic Research Program of China (Grant No.
 352 2015CB921401), National Key Research and Development Program of China (Grant No.

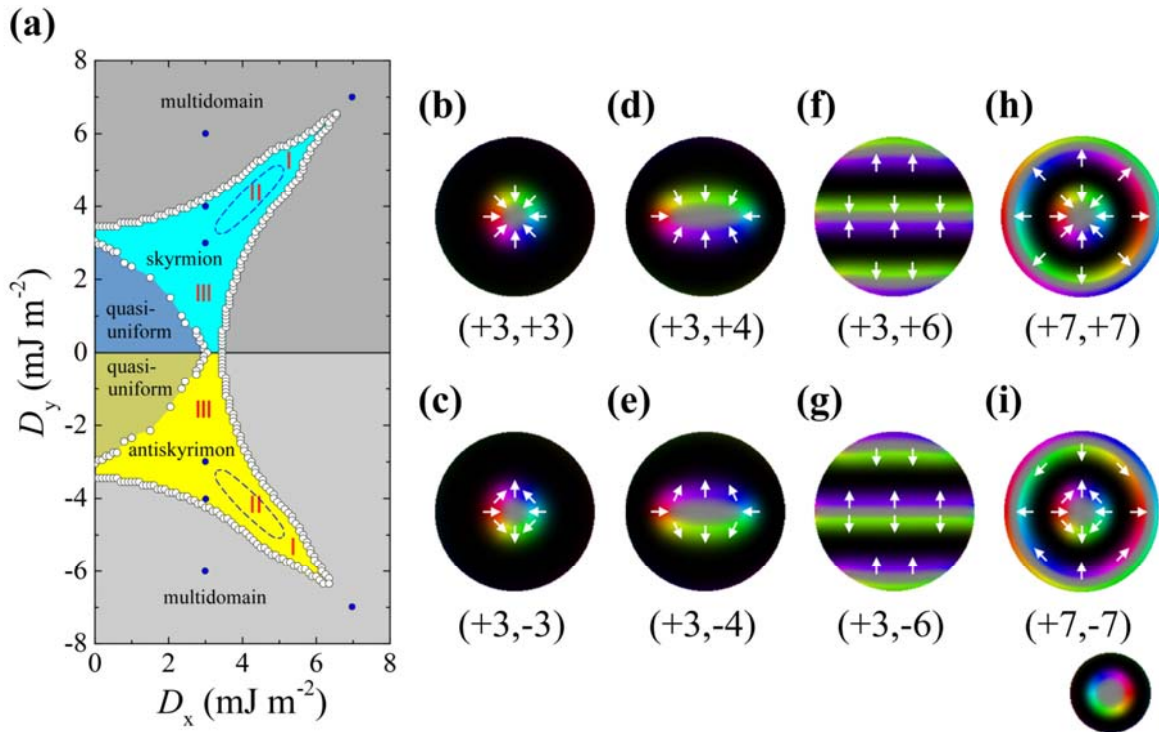
353 2016YFA0300703), National Natural Science Foundation of China (Grants No. 11474066 and No.
 354 11434003), and the Program of Shanghai Academic Research Leader (No. 17XD1400400). Work at
 355 UCD was supported by the UC Office of the President Multicampus Research Programs and
 356 Initiatives (MRP-17-454963) (G.C.) and the US NSF (DMR-1610060) (K.L.). Work at LBL was
 357 supported by the Office of Science, Office of Basic Energy Sciences, Scientific User Facilities
 358 Division, of the U.S. Department of Energy under Contract No. DE-AC02—05CH11231.



360 FIG. 1. Skyrmion and antiskyrmion configurations corresponding to isotropic and anisotropic DMI,
361 respectively. (a) and (b), Schematic diagrams of isotropic and anisotropic DMI. Red balls indicate
362 atomic spins at the interface while blue arrows indicate the DM vectors. (c) and (d), Arrows-array
363 representation of skyrmion and antiskyrmion spin configurations. (e) and (f), Construction recipes
364 for skyrmion and antiskyrmion in order parameter space. Note that panel c and d can be derived from
365 panel e and f through stereographic projection. In panel c-f, different colors of the arrows correspond
366 to different angles between the spins and normal direction of the interface.



367
 368 FIG. 2. Isolated antiskyrmion in a nanodisk (diameter, 80 nm) in presence of anisotropic DMI with
 369 $D_x = -D_y$. (a) Total micromagnetic energy (including the DMI, exchange, dipolar and anisotropy
 370 energies) for different states of the nanodisk as a function of D_x along the line of $D_x = -D_y$ in
 371 (D_x, D_y) space. Dashed lines indicate that the corresponding states are unstable in the simulations
 372 and tends to relax to more stable states. D' and D'' indicate points where two different states are
 373 energetically degenerate. Insets show examples of relaxed magnetization distributions of the
 374 nanodisk for several points in the graph. (b) Magnetization distribution for an antiskyrmion ground
 375 state with $D_x = -D_y = 4 \text{ mJ m}^{-2}$. Red, white and blue colours indicate out-of-plane magnetization
 376 distribution as shown in the color bar, as used throughout the paper. Black arrows highlight the
 377 in-plane orientation of spins.



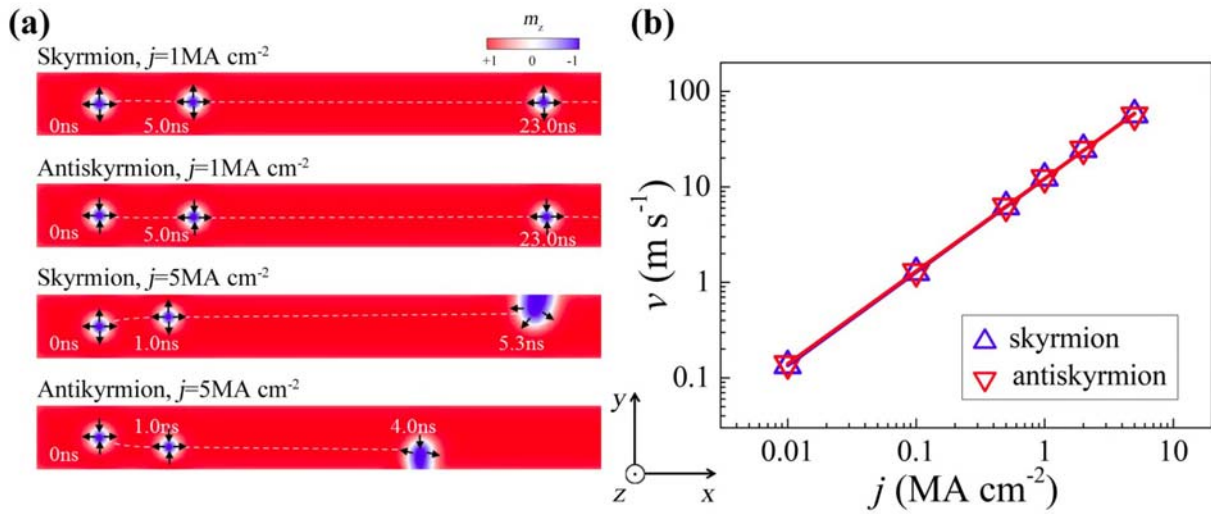
379

380 FIG. 3. Phase diagram of skyrmion and antiskyrmion states in (D_x, D_y) space. (a) Phase diagram
 381 for a 80nm wide, 0.4nm thick cobalt nanodisk on a substrate inducing DMI in zero field. Regions
 382 coloured cyan, yellow and green correspond to quasi-uniform, skyrmion/antiskyrmion and
 383 multidomain states, respectively. White dots in a show the phase boundary obtained from the
 384 simulations. The blue dashed loops outline regions labeled \square where skyrmion and antiskyrmions are
 385 the most stable states. In regions labeled \square (\square) the energy of multidomain (quasi-uniform) states is
 386 lower than that of skyrmion/antiskyrmion states. (b)-(i), Representative magnetization distribution
 387 graphs for (D_x, D_y) values listed under each graph (in units of mJ m^2), blue dots in a mark the
 388 corresponding phase diagram coordinates. The relationship between different colors and in-plane
 389 magnetization directions is shown in the colour wheel, and in-plane spin orientations are highlighted
 390 by white arrow

391

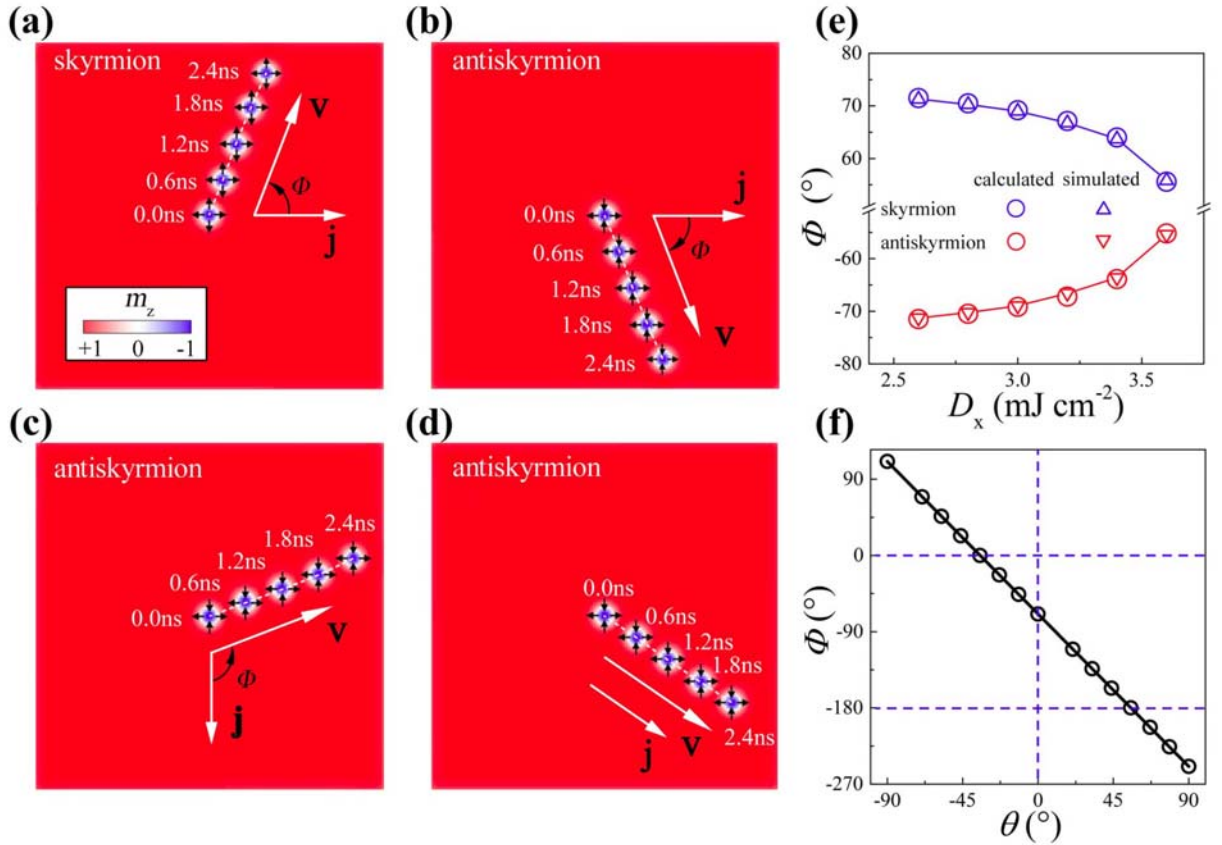
392

393



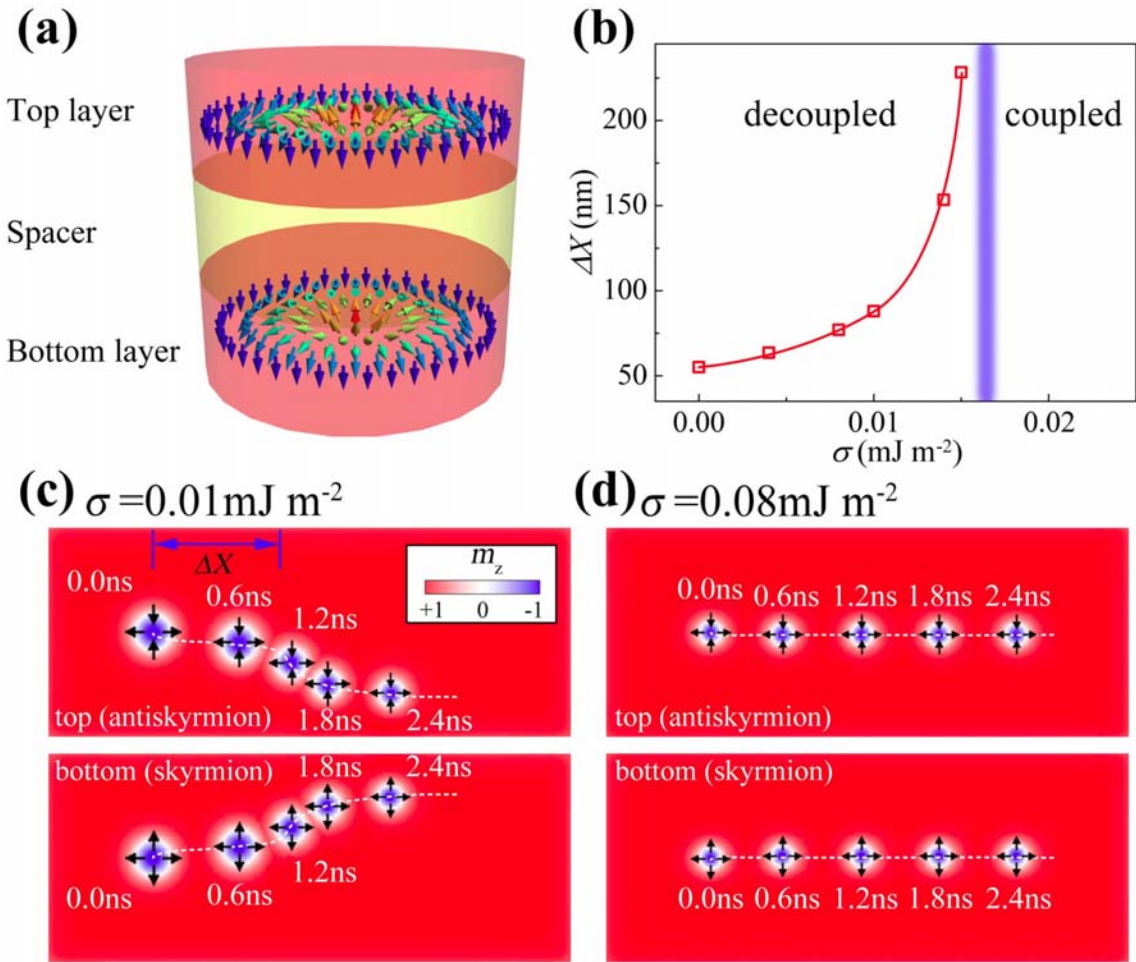
395

396 FIG. 4. Current-induced motion of skyrmions and antiskyrmions on nanotracks. (a) Current-driven
 397 motion of skyrmions and antiskyrmions on nanotracks for different current densities. White dashed
 398 lines indicates trajectories and black arrows show the in-plane spin orientations in the perimeters of
 399 the skyrmion/antiskyrmion. (b) The simulated Skyrmion and antiskyrmion velocity as a function of
 400 current density. The velocities of skyrmions and antiskyrmions are almost equal at all current
 401 densities.



402

403 FIG. 5. Anisotropic antiskyrmion Hall effect. (a) Skyrmion motion trajectory with current along the x
 404 axis. (b)-(d) Antiskyrmion motion trajectories with the current direction at $\theta = 0^\circ$, -90° and -34.5°
 405 to the x-axis, respectively. White dashed lines in panel a-d represent the trajectories. (e) Skyrmion and
 406 antiskyrmion Hall angles Φ as a function of DMI constant. (f) Antiskyrmion Hall angle Φ as a
 407 function of current direction θ , solid line is a linear fit. In these simulations the size of the
 408 nanotrack is $300 \times 300 \times 0.4 \text{ nm}^3$, and the applied current density is 10 MA cm^{-2} .



409

410 FIG. 6. Current-induced motion of ferromagnetically coupled antiskyrmion-skyrmion pairs. (a)
 411 Illustration of a antiskyrmion-skyrmion pair in a bilayer system. (b) decomposition distance ΔX as a
 412 function of the interface coupling strength σ . The red line is a guide to eye. The blue shadowed line
 413 represents the critical value of σ above which the antiskyrmion-skyrmion pair remains coupled. (c)
 414 Current induced motion of antiskyrmion-skyrmion pair which is not sufficiently coupled, at coupling
 415 strength $\sigma = 0.01 \text{ mJ m}^{-2}$. (d) Current induced motion of antiskyrmion-skyrmion pair that remains
 416 coupled, at sufficient coupling strength $\sigma = 0.08 \text{ mJ m}^{-2}$. Dashed lines in panel c and d represent
 417 the trajectories. Size of the coupled bilayer nanotrack is $200 \times 80 \times 1.2 \text{ nm}^3$, current density is
 418 5 MA cm^{-2} , and $D_x = 3 \text{ mJ m}^{-2}$.

-
-
- [1] H.-B. Braun, Topological effects in nanomagnetism: from superparamagnetism to chiral quantum solitons. *Advances in Physics*, **61**, 1 (2012).
- [2] R. Hertel, S. Gliga, M. Fähnle, and C. M. Schneider Ultrafast Nanomagnetic Toggle Switching of Vortex Cores. *Phys. Rev. Lett.* **98**, 117201 (2007).
- [3] H.B. Braun, Thermally activated magnetization reversal in elongated ferromagnetic particles. *Phys. Rev. Lett.* **71**, 3557 (1993).
- [4] N. Nagaosa, and Y. Tokura, Topological properties and dynamics of magnetic skyrmions. *Nat. Nanotech.* **8**, 899 (2013).
- [5] M. J. Benitez, A. Hrabec, A. P. Mihai, T. A. Moore, G. Burnell, D. McGrouther, C. H. Marrows, and S. McVitie, Magnetic microscopy and topological stability of homochiral Néel domain walls in a Pt/Co/AlO_x trilayer. *Nat. Commun.* **6**, 8957 (2015).
- [6] T. H. R. Skyrme, A unified field theory of mesons and baryons. *Nucl. Phys.* **31**, 556 (1962).
- [7] A. Bogdanov, and A. Hubert, Thermodynamically stable magnetic vortex states in magnetic crystals. *J. Magn. Magn. Mater.* **138**, 255 (1994).
- [8] U. K. Roszler, A. N. Bogdanov, and C. Pfleiderer, Spontaneous skyrmion ground states in magnetic metals. *Nature* **442**, 797 (2006).
- [9] F. Jonietz, S. Mühlbauer, C. Pfleiderer, A. Neubauer, W. Münzer, A. Bauer, T. Adams, R. Georgii, P. Böni, R. A. Duine, K. Everschor, M. Garst, and A. Rosch, Spin Transfer Torques in MnSi at Ultralow Current Densities. *Science* **330**, 1648 (2010).

-
-
- [10]X.Z. Yu, N. Kanazawa, W.Z. Zhang, T. Nagai, T. Hara, K. Kimoto, Y. Matsui, Y. Onose, and Y. Tokura, Skyrmion flow near room temperature in an ultralow current density. *Nature Commun.* **3**, 988 (2012).
- [11]J. Sampaio, V. Cros, S. Rohart, A. Thiaville, and A. Fert, Nucleation, stability and current-induced motion of isolated magnetic skyrmions in nanostructures. *Nat. Nanotech.* **8**, 839 (2013).
- [12]A. Fert, V. Cros, and J. Sampaio, Skyrmions on the track. *Nat. Nanotech.* **8**, 152 (2013).
- [13]I. E. Dzyaloshinskii, Thermodynamic theory of "weak" ferromagnetism in antiferromagnetic substances. *Sov. Phys. JETP* **5**, 1259 (1957).
- [14]T. Moriya, Anisotropic superexchange interaction and weak ferromagnetism. *Phys. Rev.* **120**, 91 (1960).
- [15]A. Fert and P. M. Levy, Role of anisotropic exchange interactions in determining the properties of spin-glasses. *Phys. Rev. Lett.* **44**, 1538 (1980).
- [16]A. Fert, Magnetic and transport properties of metallic multilayers. *Metallic Multilayers.* **59–60**, 439 (1990).
- [17]A. Crépieux, and C. Lacroix, Dzyaloshinskii–Moriya interactions induced by symmetry breaking at a surface. *J. Magn. Magn. Mater.* **182**, 341 (1998).
- [18]S. Heinze, K. von Bergmann, M. Menzel, J. Brede, A. Kubetzka, R. Wiesendanger, G. Bihlmayer, and S. Blügel, Spontaneous atomic-scale magnetic skyrmion lattice in two dimensions. *Nat. Phy.* **7**, 713 (2011).

-
-
- [19]L. Sun, R. X. Cao, B. F. Miao, Z. Feng, B. You, D. Wu, W. Zhang, An Hu, and H. F. Ding, Creating an artificial two-dimensional skyrmion crystal by nanopatterning. *Phys. Rev. Lett.* **110**, 167201 (2013).
- [20]J. Li, A. Tan, K.W. Moon, A. Doran, M.A. Marcus, A.T. Young, E. Arenholz, S. Ma, R.F. Yang, C. Hwang, and Z.Q. Qiu, Tailoring the topology of an artificial magnetic skyrmion, *Nat. Commun.* **5**, 4704 (2014).
- [21]D. A. Gilbert, B. B. Maranville, A. L. Balk, B. J. Kirby, P. Fischer, D. T. Pierce, J. Unguris, J. A. Borchers, and K. Liu, Realization of ground-state artificial skyrmion lattices at room temperature. *Nat. Commun.* **6**, 8462 (2015).
- [22]B.A.Ivanov, V.A.Stephanovich, and A.A.Zhmudskii, Magnetic vortices: The microscopic analogs of magnetic bubbles. *J. Magn. Magn. Mater.* **88**, 116 (1990).
- [23]Ar. Abanov, and V.L. Pokrovsky, Skyrmion in a real magnetic film. *Phys. Rev. B* **58**, R8889(R) (1998).
- [24]X. Z. Yu, Y. Onose, N. Kanazawa, J. H. Park, J. H. Han, Y. Matsui, N. Nagaosa, and Y. Tokura, Real-space observation of a two-dimensional skyrmion crystal. *Nature* **465**, 901 (2010).
- [25]X. Z. Yu, N. Kanazawa, Y. Onose, K. Kimoto, W. Z. Zhang, S. Ishiwata, Y. Matsui, and Y. Tokura, Near room-temperature formation of a skyrmion crystal in thin-films of the helimagnet FeGe. *Nat. Mater.* **10**, 106 (2011).
- [26]G. Chen, A. Mascaraque, A. T. N'Diaye and A. K. Schmid, Room temperature skyrmion ground state stabilized through interlayer exchange coupling. *Appl. Phys. Lett.* **106**, 242404 (2015).

-
-
- [27] W. Jiang, P. Upadhyaya, W. Zhang, G. Yu, M. B. Jungfleisch, F. Y. Fradin, J. E. Pearson, Y. Tserkovnyak, K. L. Wang, O. Heinonen, S. G. E. te Velthuis, and A. Hoffmann, Blowing magnetic skyrmion bubbles. *Science* **349**, 283 (2015).
- [28] C. Moreau-Luchaire, C. Moutafis, N. Reyren, J. Sampaio, C. A. F. Vaz, N. Van Horne, K. Bouzheouane, K. Garcia, C. Deranlot, P. Warnicke, P. Wohlhüter, J.-M. George, M. Weigand, J. Raabe, V. Cros, and A. Fert, Additive interfacial chiral interaction in multilayers for stabilization of small individual skyrmions at room temperature. *Nat. Nanotech.* **11**, 444 (2016).
- [29] O. Boulle, J. Vogel, H. Yang, S. Pizzini, D. de Souza Chaves, A. Locatelli, T. Onur Menteş, A. Sala, L. D. Buda-Prejbeanu, O. Klein, M. Belmeguenai, Y. Roussigné, A. Stashkevich, S. Mourad Chérif, L. Aballe, M. Foerster, M. Chshiev, S. Auffret, I. Mihai Miron, and G. Gaudin, Room-temperature chiral magnetic skyrmions in ultrathin magnetic nanostructures. *Nat. Nanotech.* **11**, 449 (2016).
- [30] R. Wiesendanger, Nanoscale magnetic skyrmions in metallic films and multilayers: a new twist for spintronics. *Nature Reviews Materials* **1**, 16044 (2016).
- [31] S. Woo, K. Litzius, B. Krüger, M.-Y. Im, L. Caretta, K. Richter, M. Mann, A. Krone, R. Reeve, M. Weigand, P. Agrawal, P. Fischer, M. Kläui, and G. S. D. Beach, Observation of room temperature magnetic skyrmions and their current-driven dynamics in ultrathin films. *Nat. Mater.* **15**, 501 (2016).
- [32] W. Legrand, D. Maccariello, N. Reyren, K. Garcia, C. Moutafis, C. Moreau-Luchaire, S. Collin, K. Bouzheouane, V. Cros, and A. Fert, Room-Temperature Current-Induced Generation and Motion of sub-100 nm Skyrmions, *Nano Lett.* **17**, 2703 (2017).

-
-
- [33]P.-J. Hsu, A. Kubetzka, A. Finco, N. Romming, K. von Bergmann, and R. Wiesendanger, Electric-field-driven switching of individual magnetic skyrmions. *Nat. Nanotech.* **12**, 123 (2017).
- [34]C. Hanneken, F. Otte, A. Kubetzka, B. Dupé, N. Romming, K. von Bergmann, R. Wiesendanger, S. Heinze, Electrical detection of magnetic skyrmions by tunneling non-collinear magnetoresistance. *Nat. Nanotech.* **10**, 1039 (2015).
- [35]J. Zang, M. Mostovoy, J. H. Han, and N. Nagaosa, Dynamics of skyrmion crystals in metallic thin films. *Phys. Rev. Lett.* **107**, 136804 (2011).
- [36]J. Iwasaki, M. Mochizuki, and N. Nagaosa, Universal current-velocity relation of skyrmion motion in chiral magnets. *Nat. Commun.* **4**, 1463 (2013).
- [37]J. Iwasaki, M. Mochizuki, and N. Nagaosa, Current-induced skyrmion dynamics in constricted geometries. *Nat. Nanotech.* **8**, 742 (2013).
- [38]K. Everschor-Sitte, and M. Sitte, Real-space Berry phases: Skyrmion soccer. *J. Appl. Phys.* **115**, 172602 (2014).
- [39]C. Reichhardt, D. Ray, and C. J. O. Reichhardt, Collective transport properties of driven skyrmions with random disorder. *Phys. Rev. Lett.* **114**, 217202 (2015).
- [40]C. Reichhardt, D. Ray, and C. J. O. Reichhardt, Quantized transport for a skyrmion moving on a two-dimensional periodic substrate. *Phys. Rev. B* **91**, 104426 (2015).
- [41]J. Muller, and A. Rosch, Capturing of a magnetic skyrmion with a hole. *Phys. Rev. B* **91**, 054410 (2015).
- [42]S.-Z. Lin, Edge instability in a chiral stripe domain under an electric current and skyrmion generation. *Phys. Rev. B* **94**, 020402(R) (2016).

-
- [43]R. Tomasello, E. Martinez, R. Zivieri, L. Torres, M. Carpentieri, and G. Finocchio, A strategy for the design of skyrmion racetrack memories. *Scientific Reports* **4**, 6784 (2014).
- [44] A. Thiele, A. Steady-State Motion of Magnetic Domains. *Phys. Rev. Lett.* **30**, 230 (1972).
- [45]W. Jiang, X. Zhang, G. Yu, W. Zhang, X. Wang, M. B. Jungfleisch, J. E. Pearson, X. Cheng, O. Heinonen, K. L. Wang, Y. Zhou, A. Hoffmann, and S. G. E. te Velthuis, Direct observation of the skyrmion Hall effect. *Nat. Phys.* **13**, 162 (2017).
- [46]K. Litzius, I. Lemesh, B. Krüger, P. Bassirian, L. Caretta, K. Richter, F. Büttner, K. Sato, O. A. Tretiakov, J. Förster, R. M. Reeve, M. Weigand, I. Bykova, H. Stoll, G. Schütz, G. S. D. Beach, and Mathias Kläui Skyrmion Hall effect revealed by direct time-resolved X-ray microscopy. *Nat. Phys.* **13**, 170 (2017).
- [47]X. Zhang, Y. Zhou and E. Motohiko, Magnetic bilayer-skyrmions without skyrmion Hall effect. *Nat. Commun.* **7**, 10293 (2016).
- [48]J. Barker, and O. A. Tretiakov, Static and dynamical properties of antiferromagnetic skyrmions in the presence of applied current and temperature. *Phys. Rev. Lett.* **116**, 147203 (2016).
- [49]A. N. Bogdanov, U. K. Röbler, M. Wolf, and K.H. Müller, Magnetic structures and reorientation transitions in noncentrosymmetric uniaxial antiferromagnets. *Phys. Rev. B* **66**, 214410 (2002).
- [50]T. Okubo, S. Chung, and H. Kawamura, Multiple- q States and the Skyrmion Lattice of the Triangular-Lattice Heisenberg Antiferromagnet under Magnetic Fields. *Phys. Rev. Lett.* **108**, 017206 (2012).
- [51]W. Koshibae, and N. Nagaosa, Creation of skyrmions and antiskyrmions by local heating. *Nat. Commun.* **5**, 5148 (2014).

-
-
- [52]W. Koshibae, and N. Nagaosa, Theory of antiskyrmions in magnets. *Nat. Commun.* **7**, 10542 (2016).
- [53]A. N. Bogdanov and D. A. Yablonsky, *Sov. Phys. JETP* **68**, 101 (1989).
- [54]M. Heide, G. Bihlmayer, and S. Blügel, Dzyaloshinskii-Moriya interaction accounting for the orientation of magnetic domains in ultrathin films: Fe/W (110). *Phys. Rev. B* **78**, 140403 (2008).
- [55]L. Camosi, S. Rohart, O. Fruchart, S. Pizzini, M. Belmeguenai, Y. Roussigné, A. Stachkevitch, S. Mourad Chérif, L. Ranno, M. De Santis, and J. Vogel, Anisotropic Dzyaloshinskii-Moriya Interaction in ultra-thin epitaxial Au/Co/W(110). arXiv:1701.05062 [cond-mat.mtrl-sci].
- [56]G. Chen, J. Zhu, A. Quesada, J. Li, A.T. N'Diaye, Y. Huo, T.P. Ma, Y. Chen, H.Y. Kwon, C. Won, Z.Q. Qiu, A.K. Schmid, and Y.Z. Wu, Novel Chiral Magnetic DomainWall Structure in Fe/Ni/Cu(001) Films. *Phys. Rev. Lett.* **110**, 177204 (2013).
- [57]G. Chen, T.P. Ma, A.T. N'Diaye, H.Y. Kwon, C. Won, Y.Z. Wu, and A.K. Schmid, Tailoring the chirality of magnetic domain walls by interface engineering. *Nat. Commun* **4**,2671 (2013).
- [58]M. J. Donahue, and D. G. Porter, OOMMF user's guide, version 1.2a5. *Interagency Report NISTIR 6376* (1999).
- [59]<http://www.lps.u-psud.fr/spip.php?article2252>
- [60]S. Rohart, and A. Thiaville, Skyrmion confinement in ultrathin film nanostructures in the presence of Dzyaloshinskii-Moriya interaction. *Phys. Rev. B* **88**, 184422(2013).
- [61]A. A. Zhmudskii and B. A. Ivanov, *Low Temp. Phys.* **22**, 347 (1996).
- [62]See Supplemental Materials.

[63]Ajaya K. Nayak, Vivek Kumar, Tianping Ma, Peter Werner, Eckhard Pippel, Roshnee Sahoo, Franoise Damay, Ulrich K. Rößler, Claudia Felser & Stuart S. P. Parkin, Magnetic antiskyrmions above room temperature in tetragonal Heusler materials. *Nature* (2017) doi:10.1038/nature23466.

[64]Markus Hoffmann, Bernd Zimmermann, Gideon P. Müller, Daniel Schürhoff, Nikolai S. Kiselev, Christof Melcher & Stefan Blügel, Antiskyrmions stabilized at interfaces by anisotropic Dzyaloshinskii-Moriya interactions. *Nat. Commun.* **8**, 308 (2017).